

Designer Edge States in Fractional Polarization Insulators

Wei Jie Chan, Pei-Hao Fu,* L. K. Ang, and Yee Sin Ang†
*Science, Mathematics and Technology (SMT), Singapore University of
 Technology and Design (SUTD), 8 Somapah Road, Singapore 487372*

We theoretically investigated the topological-protected edge states (TESs) in an anisotropic honeycomb lattice with mirror and chiral symmetries, characterized by an alternative topological invariant - *fractional polarization* (FP), rather than the conventional Chern number. This system termed an FP insulator is a potential platform for edge-state engineering due to its disconnected TESs. These disconnected and robust TESs are susceptible to perturbative chiral symmetry-breaking terms which can generate various patterns including the vanishing helical, spin-polarized, and chiral TESs. Moreover, helical and chiral TES can be achieved by the finite size effect, not possible from the aforementioned terms alone. The demonstration of these various TES in an FP-insulator offers an alternative route in designing reconfigurable two-dimensional nanoelectronic devices.

I. INTRODUCTION

Edge states protected by non-trivial bulk topology [1] are robust against defects and symmetry-preserved backscattering [2, 3]. Usually, the topological-protected edge states (TESs) are guaranteed by the non-vanishing Berry curvature, and their number is related to the Chern number due to the bulk-boundary correspondence [2, 3]. Alternatively, the TESs can still be characterized by another bulk topological invariant, i.e. the fractional edge or surface polarization even with a vanishing Chern number [4, 5]. This fractional polarization (FP) requires a mirror and chiral symmetry [6, 7] and is related to the quantized Zak phase in time-reversal and inversion symmetric systems [6, 8]. Recently, this is commonly realized on a two-dimensional (2D) square lattice with anisotropic hopping amplitudes [9–12], 2D SSH models [13–15] such as in A_3B monolayers [16] and in anisotropic 2D honeycomb lattices with a zero Chern number [7, 17, 18].

Unlike the usual isotropic model in the well-celebrated graphene [19] and other metamaterials [20], the anisotropic model has a modified nearest neighbor (NN) hopping term and is a tunable parameter [21, 22]. This tunability merges two Dirac cones in the band structure and results in the topological phase transition [see Fig. 1(b)] from band-inversion, semi-Dirac, and insulating phase characterized by different transport signatures [23, 24] and of potential in designing valleytronics device [25–27]. Apart from photonic [28], polariton materials [29] and α -dice lattice [30–32], the anisotropic honeycomb lattices are also expected in anisotropic graphene [33] and phosphorene [7, 34], monolayer arsenene [35] and silicene oxide [36]. However, the insulating phase here is not a conventional one, which supports these disconnected TESs [7, 33, 34, 37], and therefore is termed the FP-insulating phase. Unlike the Zak-insulating anisotropic graphene [4, 5], the invariant characterizing the presence of the TES is attributed to the quantized FP in phos-

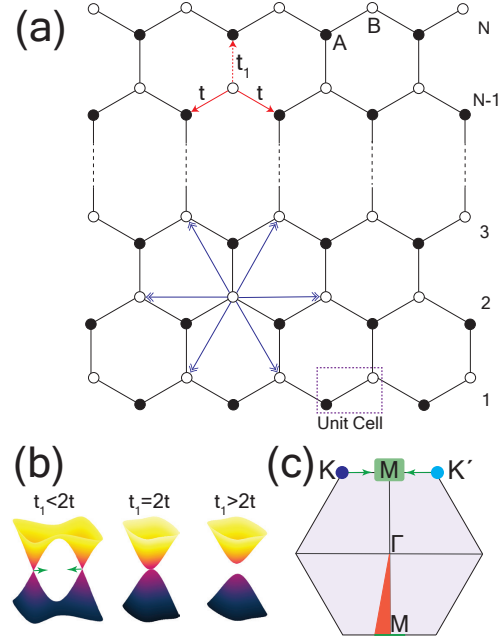


FIG. 1: A schematic of a semi-Dirac hexagonal lattice model with two sublattices with (next-) nearest-neighbor hoppings denoted by red (blue) arrows in (a). One of the nearest-neighbor hopping terms is anisotropic with $t_1 \neq t$. The low-energy effective dispersion governed by t_1/t is shown in (b). The merging of the K and K' point into the M point is shown within the first Brillouin zone in (c). The fundamental triangle after the merger for $t_1 > 2t$ is illustrated as the orange triangle.

phorene due to the mirror symmetries [34]. Furthermore, the quantization of FP is robust even under perturbative chiral-symmetry breaking terms [7]. This agrees with [17] in the presence of small chiral symmetry-breaking terms in the insulating phase and a vanishing bulk topological invariant.

The aim of this work is to highlight and address the underlying mechanism behind the different possible TES within the FP-insulating phase, which is guaranteed by

* peihao_fu@sutd.edu.sg
 † yeemin_ang@sutd.edu.sg

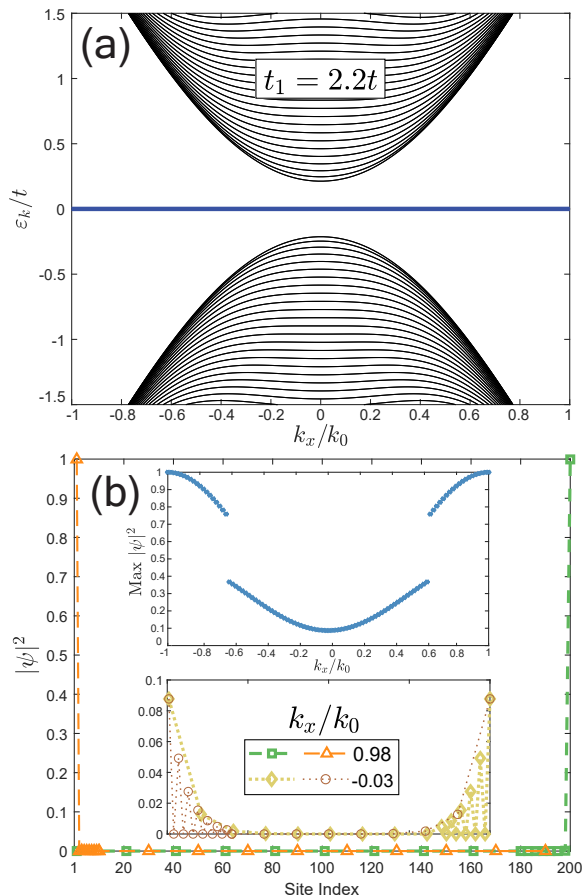


FIG. 2: Topological edge states (TESs) isolated from the bulk bands from Eq. (13) with a semi-open boundary condition (sOBC) are plotted with ϵ_k/t (with subscript k as k_x) against k_x/k_0 in (a) with $k_0 = \pi/(a\sqrt{3})$ and $t_1 = 2.2t$ in the presence of NN hoppings only. The total number of sites along the OBC direction (y) is 200 and the value $t_1 = 2.2t$ is fixed for the remainder of the figures. The wavefunction probability $|\psi|^2$ against site index at momenta k_x/k_0 are shown in figure (b) with its bottom inset. The top inset illustrates the regions of localized/delocalized TES across the Brillouin zone (BZ).

the mirror symmetries as long as the bulk gap remains open. This allows us to utilize perturbative chiral (sublattice) symmetry-breaking terms such as spin-orbit coupling (SOC), staggering potential, and exchange proximity effect to realize various TES including the vanishing helical, spin-polarized, and chiral states. The additional underlying symmetry can also explain the origin of the flat and the two helical TES spectra. Notably, the finite-size effect can gap out the zero-energy states around the minimal bulk band gap to generate a helical or chiral TES, not possible with the aforementioned chiral symmetry-breaking parameters alone.

The remainder of this paper is organized as follows. In Section II, the FP corresponding to the edge state

of the Hamiltonian of the anisotropic honeycomb lattice is introduced. The engineering of the TESs is demonstrated in Section III by considering perturbative chiral symmetry-breaking terms and the finite-size effect. The conclusion is drawn in Section IV.

II. MODEL

A. Tight-Binding Model

The anisotropic honeycomb lattice in Fig. 1(a) has two nearest neighbors (NN) hopping, t (red arrows), a differing third NN hopping, t_1 (red broken arrow) governed by H_0 , and an inversion symmetry-breaking next-nearest neighbors (NNN) intrinsic SOC contribution term (blue arrows) governed by H_{SOC} such that

$$H_0 = \sum_{\langle i,j \rangle, s} t_{ij} c_{i,s}^\dagger c_{j,s} \quad (1)$$

$$H_{\text{SOC}} = i\lambda_{\text{SO}} \sum_{\langle\langle j,j' \rangle\rangle, s, s'} \nu_{jj'} c_{j,s}^\dagger s_z^{s,s'} c_{j',s'} \quad (2)$$

where the hopping term between site j and j' is denoted by $t_{jj'}$. The SOC coefficient is λ_{SO} with an orientation coefficient $\nu_{jj'} = 2(\mathbf{d}_j \times \mathbf{d}_{j'})/\sqrt{3} = \pm 1$, with the unit vector along the bonds between site j and j' as \mathbf{d}_j and the spin vector along z between spin s and s' as the spin Pauli matrix $\mathbf{s}_z^{s,s'}$. Additionally, we further include an onsite staggered potential H_{Stag} and a time-reversal breaking exchange proximity field H_{Ex}

$$H_{\text{Stag}} = \sum_j \lambda_{\Delta,j} c_j^\dagger c_j, \quad (3)$$

$$H_{\text{Ex}} = \sum_{j,s,s'} \lambda_{\text{Ex},j} c_{j,s}^\dagger s_z^{s,s'} c_{j,s'}, \quad (4)$$

where $\lambda_{\Delta,j} = \pm 1$ denotes A (+) or B (-) sublattice, $\lambda_{\text{Ex},j} = \lambda_{\text{FM}}$ which denotes a ferromagnetic (FM) exchange effect, or antiferromagnetic (AFM), $\lambda_{\text{AFM},j}$ proximity effect.

After a Fourier transformation, the Hamiltonian in momentum space with the basis of $(c_{A,\uparrow}, c_{B,\uparrow}, c_{A,\downarrow}, c_{B,\downarrow})^T$ is (see Appendix A for details)

$$H_{s_z} = \begin{bmatrix} m_{s_z} + s_z \lambda_{\text{FM}} & f_1 - if_2 \\ f_1 + if_2 & -m_{s_z} + s_z \lambda_{\text{FM}} \end{bmatrix}, \quad (5)$$

where $m_{s_z} = s_z(f_{\text{SO}} + \lambda_{\text{AFM}}) + \lambda_{\Delta}$ and the following

terms are

$$f_1 = t_1 \cos(k_y a) + 2t \cos\left(\frac{\sqrt{3}}{2} k_x a\right) \cos\left(\frac{k_y a}{2}\right), \quad (6)$$

$$f_2 = -t_1 \sin(k_y a) + 2t \cos\left(\frac{\sqrt{3}}{2} k_x a\right) \sin\left(\frac{k_y a}{2}\right), \quad (7)$$

$$f_{\text{SO}} = -2\lambda_{\text{SO}} \left[\sin\left(\sqrt{3} k_x a\right) - 2 \cos\left(\frac{3k_y a}{2}\right) \sin\left(\frac{\sqrt{3} k_x a}{2}\right) \right]. \quad (8)$$

Eq. (5) can be decomposed into $H_{s_z} = H_0 + H_C$, where $H_C = m_{s_z} \sigma_z + s_z \lambda_{\text{FM}} \sigma_0$, consist of all the diagonal terms, with the Pauli matrices denoted as σ_j , for $j \in \{0, x, y, z\}$, breaks chiral (sublattice) symmetry with $\mathcal{C} = \sigma_z$ and $\mathcal{C}^{-1} H_{s_z}(\mathbf{k}) \mathcal{C} \neq -H_{s_z}(\mathbf{k})$. Eq. (5) obey $\mathcal{M}_{x,y}$ symmetry and it is sufficient to study the TESs from the fundamental triangle, spanning from $k_x/k_0 = 0$ to -1 or 1 within the Brillouin zone (BZ) as highlighted in orange in Fig. 1(c) by considering the underlying mirror symmetry, $\mathcal{M}_{x,y} = i\sigma_{x,y}$ of Eq. (5),

$$\mathcal{M}_{x,y}^{-1} H_{s_z}(k_x, k_y) \mathcal{M}_{x,y} = H_{s_z}(-k_x, -k_y), \quad (9)$$

which plays a pivotal role in the bulk topological invariant of this model.

B. Topological Invariant - Fractional Polarization

The anisotropic NN hopping, t_1 induces a topological phase transition in this model, i.e. from $t_1 < 2t$ through a gapless semi-Dirac phase in $t_1 = 2t$ to an insulating phase at $t_1 > 2t$ in Fig. 1(b). This transition merges the two Dirac cones from the \mathbf{K} and \mathbf{K}' valley into a single \mathbf{M} valley as illustrated in the top half of Fig. 1(c). This produces an insulating phase with a zero Chern number after the bulk band gaps reopen when $t_1 > 2t$ [34]. In the presence of inversion and time-reversal symmetry, this was attributed to the zero Berry curvature $\Omega(k_x, k_y)$, i.e. $\Omega(k_x, k_y) = \Omega(-k_x, -k_y) = 0$ [4, 5]. The vanishing of the Chern number with a finite Berry curvature has also been shown in the absence of inversion symmetry [7, 34] in phosphorene and anisotropic square lattices [6]. However, the existence of isolated topologically protected edge states for $t_1 > 2t$ indicates that the Chern number is not suitable to describe the bulk topology [34]. This was rectified by defining a polarization term [6] to describe the bulk topology, i.e.

$$P_j = \left(\int_{\text{BZ}} A_j d^2 \mathbf{k} \right) \text{ mod } 1, \quad (10)$$

where the Berry connection is $A_{j,\pm} = -i \langle \psi_{\pm} | \partial_{k_j} | \psi_{\pm} \rangle$, with j denotes either the x or y directions for 2D and the wavefunctions of the two bands are ψ_{\pm} with $+/-$

denoting the conduction or valence band respectively s.t.

$$\psi_{\pm} = \begin{bmatrix} f_1 - i f_2 \\ \pm \varepsilon_{\mathbf{k}} - s_z \lambda_{\text{FM}} - m_{s_z} \end{bmatrix}. \quad (11)$$

Eq. (10) can still remain quantized to either 0 or $1/2$,

$$(P_x, P_y) = \left(0, \frac{1}{2} \right), \quad (12)$$

in the absence of inversion symmetry, as long as \mathcal{M}_j is present [6].

The FP is quantized in the presence of chiral symmetry and was shown to remain well-quantized in the presence of perturbative chiral symmetry-breaking terms [7]. To ensure the quantization, the terms in H_C must be small and not be comparable to t . Here, the criteria becomes $|2\lambda_{\text{SO}} + \lambda_{\text{AFM}} + \lambda_{\Delta} + \lambda_{\text{FM}}| \ll |t|$, where the maximum value of $|f_{\text{SO}}|$ is $2\lambda_{\text{SO}}$. For commonly known 2D anisotropic honeycomb lattice such as phosphorene [7], the minimal NN hopping energy is approximately 1.22eV, which imposes an upper bound of $21\lambda_0$ with $|\lambda_0| = 0.1/\sqrt{3}$. Hence, the impractically large upper bound demonstrates the perturbative nature of the H_C and ensures that the bulk band gap remains open and is within the FP-insulating phase.

C. Edge States

The TESs in an FP-insulator can be produced by applying a semi-open boundary condition (sOBC) along y s.t. the system becomes a semi-infinite zigzag (ZZ) nanoribbon. The corresponding minimal Hamiltonian block derived in Appendix B is in the basis of $(c_{1,\uparrow}, c_{2,\uparrow} \dots c_{N,\uparrow}, c_{1,\downarrow} \dots c_{N,\downarrow})^T$ with

$$H_{s_z}^{\text{edge}}(k_x) = \begin{bmatrix} \tilde{m}(+, +) & f & s_z g_{\text{SO}} & 0 \\ f^* & \tilde{m}(-, +) & t_1 & -s_z g_{\text{SO}} \\ s_z g_{\text{SO}}^* & t_1 & \tilde{m}(+, -) & f \\ 0 & -s_z g_{\text{SO}}^* & f^* & \tilde{m}(-, -) \end{bmatrix} \quad (13)$$

where the terms are $\tilde{m}(\pm, \pm) = \pm m + s_z \lambda_{\text{FM}}$, with $s_z = \pm$ for the FM interaction and

$$m = s_z (f_{\text{SO}}^{\text{edge}} + \lambda_{\text{AFM}}) + \lambda_{\Delta}; \quad (14)$$

$$f = 2t \cos\left(\sqrt{3} k_x a / 2\right); \quad (15)$$

$$f_{\text{SO}}^{\text{edge}} = 2\lambda_{\text{SO}} \sin\left(\sqrt{3} k_x a\right); \quad (16)$$

$$g_{\text{SO}} = 2\lambda_{\text{SO}} \sin\left(\sqrt{3} k_x a / 2\right), \quad (17)$$

with the boundary condition $\psi_{0,B} = \psi_{N+1,A} = 0$. Notably, these terms in Eq. (13) are of central importance in manipulating the TES configurations within the FP-insulating phase as discussed below.

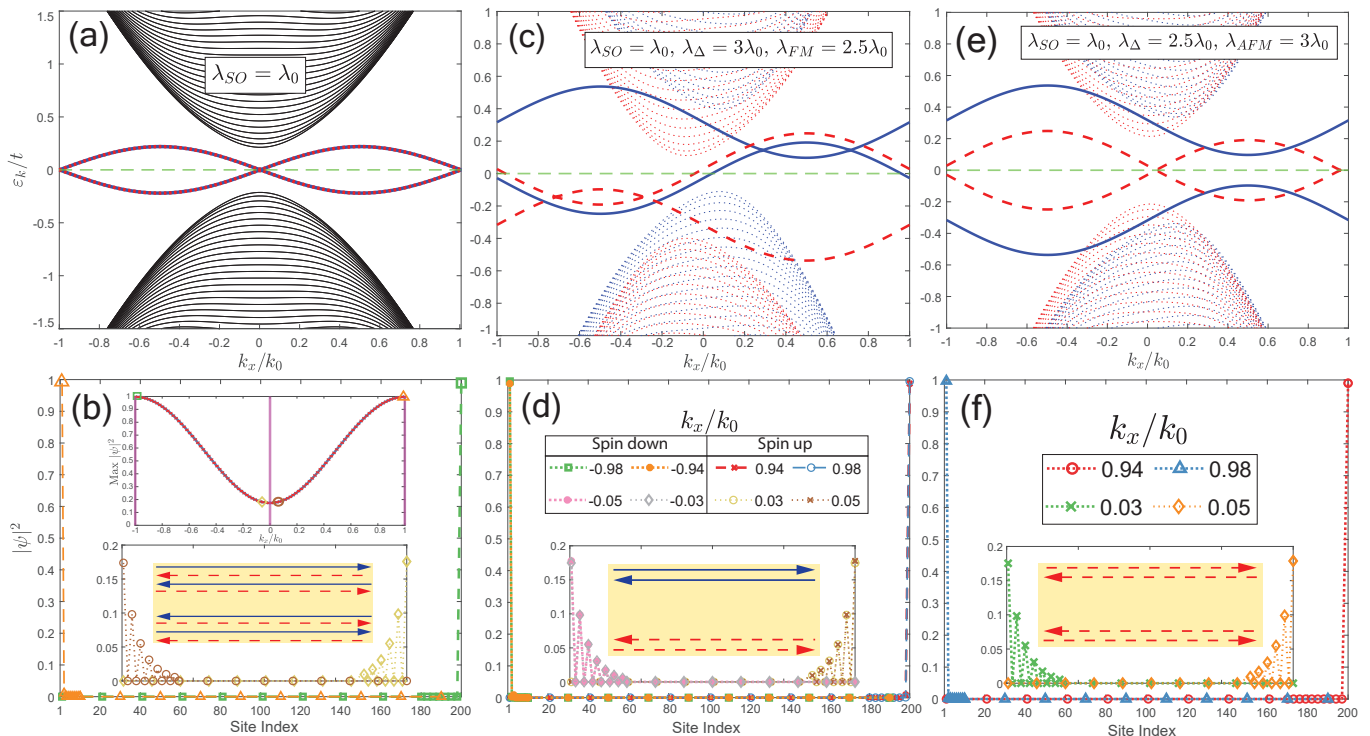


FIG. 3: The effects of spin-orbit coupling (SOC) (a), with the addition of an onsite staggering of $\lambda_{\Delta} = 3\lambda_0$ with a ferromagnetic (FM) exchange interaction with $\lambda_{FM} = 2.5\lambda_0$ (c), and the addition of an onsite staggering of $\lambda_{\Delta} = 2.5\lambda_0$ with an antiferromagnetic (AFM) exchange interaction with $\lambda_{FM} = 3\lambda_0$ (e) are shown with ϵ_k/t against k_x/k_0 at $\lambda_{SO} = \lambda_0$. The wavefunction probability is plotted against the site index in the main figure and in the bottom inset with $|\psi|^2$ against the site index for (a), (c), and (e) in (b), (d) and (f) respectively. The top inset in (b) illustrates the maximum $|\psi|^2$ against the normalized momenta k_x/k_0 with the spin-up(down) indicated as a blue line(red cross), with the purple vertical lines indicating the high symmetric points. The yellow schematic in the inset of the bottom figures illustrates the vanishing helical, spin-polarized, and chiral TESs in (b), (d), and (f) respectively.

III. EDGE STATES ENGINEERING

A. Flat Topological Edge States

The inclusion of the chiral symmetry-breaking terms in H_C such as SOC, staggering, and exchange proximity effect terms in Eq. (13), i.e. f_{SO}^{edge} , g_{SO} , λ_{Δ} , λ_{FM} and λ_{AFM} modifies the behaviors of the TES spectrum while maintaining the quantization of FP as discussed in Section II. The mechanism behind these modifications can be shown by systematically tracking the zero-energy modes and the underlying symmetries for each newly added term in Eq. (13). The order of addition is as follows - NN hoppings, SOC NNN hoppings, staggering with ferromagnetic (FM) proximity effect, and finally swapping the FM with an antiferromagnetic (AFM) interaction. Additionally, as the anisotropic NN hopping parameter t_1 only alters the bulk band gap, it is fixed at $2.2t$ to remain in the FP-insulating phase.

The flat TESs seen from the zero-energy line of Eq. (13) with anisotropic NN hoppings and $m = f_{SO}^{edge} = g_{SO} = 0$, is plotted in Fig. 2(a) with $N = 200$ and k_x/k_0 against ϵ_k/t (with subscript k as k_x), where the momenta is normalized by $k_0 = \pi/(a\sqrt{3})$. The total number of sites is fixed at $N = 200$ for both Figs. 2 and 3. This originated from the presence of chiral symmetry, $\mathcal{C} = \sigma_z$ which ensures the quantization of the 1D Zak phase along the ZZ boundaries [33]. This agrees with [7, 34], in which the flat TES is attributed to the 1D winding number. Notably, any \mathcal{C} -breaking terms break this quantization, and hence, the spectrum may no longer be flat.

The wavefunction is localized for momenta residing near $k_x/k_0 = 1$ and decays into the bulk as momenta decrease towards 0 as shown in Fig. 2(b) with the wavefunction probability $|\psi|^2$ plotted against the site index. Particularly, the orange triangle and green square (yellow diamond and brown circle) lines show the localized (delocalized) TESs with momenta $k_x/k_0 = 0.98$ (-0.03). This is reinforced by seeing that the localized (delocal-

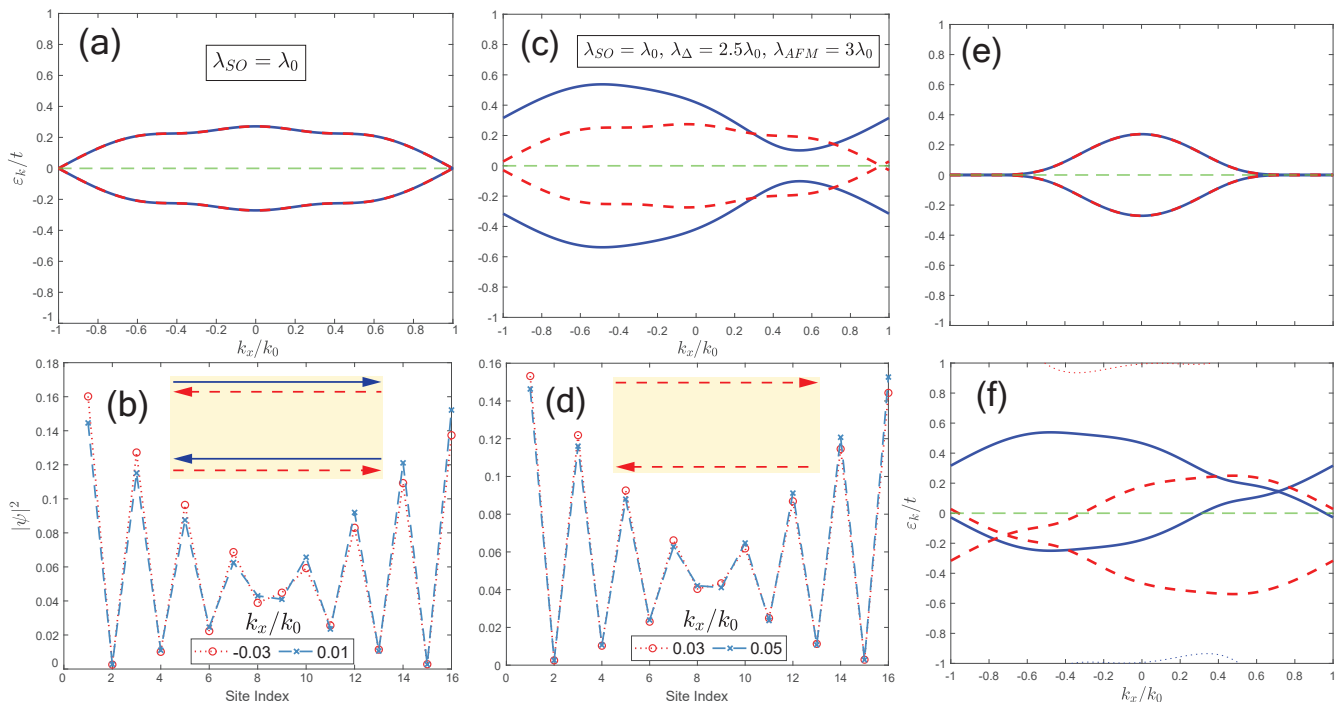


FIG. 4: The finite size effect is observed for the TES configurations in Figs. 2 and 3 by gapping the spectrum at $k_x/k_0 = 0$. This changes the zero-energy modes in (a),(c), and (e) but not in (f) with ε_k/t against k_x/k_0 . The corresponding localization behavior of the gapped is shown in (b) and (d), with the schematic showing the finite size effect induced TES along the boundaries. The normalized momenta that are chosen to describe the direction of propagation in the schematic for (b) is -0.03 (red circle) and 0.01 (blue cross), and for (d) is 0.03 (red circle) and 0.05 (blue cross).

ized) TES resides near the bulk band gap is maximum (minimum) [38] in the maximum $|\psi|^2$ against k_x/k_0 plot.

Although there is limited tunability in Fig. 2 from a fixed Eq. (15) and t_1 , the flat spectrum is a great starting point to observe the effects of SOC, onsite staggering, FM, and AFM exchange interactions.

B. Vanishing Helical Edge States

The addition of an intrinsic SOC, $\lambda_{SO} = \lambda_0$ breaks \mathcal{C} and introduced Eqs. (16) and (17) into Eq. (13). This modifies the flat spectrum in Fig. 2 to produce the vanishing helical TESs at $k_x/k_0 = 0$ and 1 in Fig. 3(a), as shown by the overlapping spin-up (solid blue lines) and spin-down (dotted red lines) bands. The zero-energy points are at $k_x/k_0 = 0, 1$ from

$$(\mathcal{M}_x \mathcal{T})^{-1} H_{s_z}^{\text{edge}}(k_x) (\mathcal{M}_x \mathcal{T}) = H_{s_z}^{\text{edge}}(-k_x). \quad (18)$$

Notably, the time-reversal symmetry that protects the symmetric points with $\mathcal{T} = i\sigma_y \mathcal{K}$ and \mathcal{K} being the complex conjugation operator, is not crucial for the quantization of FP and differs from the usual time-invariant momenta invariant [2] due to a vanishing \mathbb{Z}_2 invariant [17].

These TESs mutually oppose each other and effectively cancel each other along the boundaries as illustrated in the yellow schematic in Fig. 3(b) with blue/red arrows denoted as the spin-up/down TES, in tandem with a vanishing Chern number. The direction of propagation of TESs is determined by tracking the sign of its velocity, i.e. $v_x \propto \partial\varepsilon_k/k_x$ around the zero-energy points with the localized TESs at $k_x/k_0 = -0.98$ (green square) and 0.98 (orange triangle) in the main figure and delocalized ones at -0.03 (yellow diamond) and 0.01 (brown circle) as shown in the bottom inset. Also, the top inset shares similar behavior with the top inset in Fig. 2(b) with the spin-up/down indicated by the blue line/red cross with the delocalized/localized states residing near the momenta with the minimal/maximal bulk band gap. The markers in the top inset correspond to the momenta in Fig. 3(a) with $k_x/k_0 = -0.98$ (green square), -0.03 (yellow diamond), 0.01 (brown circle), and 0.98 (orange triangle). Notably, the addition of both onsite staggering and the Rashba effect (which breaks in-plane mirror symmetry and hence, the quantization of FP) have been shown to only shift the momenta of the zero-energy modes while retaining the vanishing spin-polarized TESs [17]. Hence, it is natural to add a time-reversal breaking exchange interaction next, to achieve a differing TES configuration while maintaining the quantization of FP.

C. Spin-Polarized Vanishing Edge States

The inclusion of both the onsite staggering potential, $\lambda_\Delta = 3\lambda_0$ and an FM exchange interaction $\lambda_{\text{FM}} = 2.5\lambda_0$ is shown in Fig. 3(c). In comparison to Fig. 3(a), the lifting of \mathcal{T} produces a spectrum that is non-spin-degenerate and has zero-energy modes that slightly deviate from the zero-energy points due to the addition of spin-splitting energy-shifting terms from the combination of both λ_Δ and $\lambda_{\text{FM/AFM}}$. While spin-splitting is already observed with just λ_Δ in Eq. (14) [17], the shifting of the zero-energy modes of each spin band is mainly dependent on $s_z\lambda_{\text{FM}}$, where the energy of the spin bands shift oppositely.

The spin-up/down TESs has positive/negative momenta which produce a vanishing spin-polarized edge state, i.e. opposing spins on opposing boundaries as illustrated in the yellow schematic diagram Fig. 3(d). This is seen from the localization behaviors of eight momenta values in Fig. 3(d), where the localization behaviors of spin-up bands have momenta at $k_x/k_0 = -0.98$ (green square) and -0.94 (orange circle), while delocalized states have momenta of -0.05 (pink circle in inset) and -0.03 (grey diamond in inset). Similarly, for the spin-down band, the momenta of the localized and delocalized states are 0.94 (red cross), 0.98 (blue circle) and 0.03 (yellow circle in inset) and 0.05 (brown cross in inset) respectively. Akin to Fig. 2, the delocalized states are located near the minima bulk band gap momenta around $k_x/k_0 = 0$. Notably, the localization of spin-up(down) states at either $N = 200(N = 1)$ highlights the presence of spin-polarization, and hence, produces a vanishing spin-polarized edge state.

D. Vanishing Chiral Edge States

The replacement of the FM interaction with the AFM interaction $\lambda_{\text{AFM}} = 3\lambda_0$ allows the realization of two mutually opposing chiral edge states in Fig. 3(e) at $\lambda_\Delta = 2.5\lambda_0$, and hence, termed a vanishing chiral edge state. Unlike the FM interaction, the AFM interaction $s_z\lambda_{\text{AFM}}$ acts in tandem with λ_Δ , towards the energy of the spin bands. Hence, this gaps the spin-up (solid blue) bands while keeping the spin-down (dashed red) states intact, realizing a spin-down version of Fig. 3(a).

The vanishing helical edge states in Fig. 3(b) turn into the vanishing chiral edge states as shown in the yellow schematic in Fig. 3(f). This is seen from the localization behavior of spin-down bands, with the delocalized states at momenta 0.03 (green cross) and 0.05 (orange diamond), and localized states at momenta 0.94 (red circle) and 0.98 (blue triangle) from Fig. 3(e).

Notably, these three cases have a vanishing TES along the boundaries, in tandem with the vanishing Chern number. Furthermore, these localization behaviors are consistent regardless of the existence of the chiral symmetry-breaking terms as compared between Fig. 2

and Fig. 3, where the delocalized/localized states are near the momenta with the minimum/maximum bulk band gap. This points out that the finite size effect can alter the TES, not possible through these chiral symmetry-breaking terms.

E. Finite Size Effect

The finite size effect is studied by restricting the total site index to $N = 16$ in Fig. 4 from $N = 200$ in Figs. 2 and 3. This effect is known to destroy the quantum spin and anomalous hall effect by producing a gap in the TES spectrum [38–41] due to the coupling of TES wavefunctions across boundaries as the total N is reduced [42]. However, the size quantization in Fig. 4(a) and (c) produce helical and chiral TESs respectively by gapping out the zero-energy crossing at $k_x/k_0 = 0$ in Fig. 3(a) and (e), not possible from the addition of the chiral symmetry-breaking terms alone. The coupling of TESs across boundaries is shown by observing that the wavefunction probability around $k_x/k_0 = 0$ decays across the site from $N = 1$ to $N = 16$ in both Fig. 4(b) and (d). Hence, unlike for the quantum spin and anomalous hall effect [38, 39], the finite size effect creates helical and chiral TESs as shown in the yellow schematic in the inset from the zero-energy modes $k_x/k_0 = \pm 1$.

Similarly, the flat spectrum in Fig. 2 produces a gap centered around $k_x/k_0 = 0$ due to the finite size effect as shown in the spectrum in Fig. 4(e). Finally, the vanishing spin-polarized TES in Fig. 3(c) is shown to be not susceptible to the finite size effect in Fig. 4(f) as the zero-energy crossings are well-localized with its momenta away from the minimum bulk band gap.

IV. CONCLUSION

In essence, the mechanism of engineering topological edge states (TESs) is studied within the fractional-polarized (FP)-insulating phase in an anisotropic honeycomb lattice. This occurs when the anisotropic hopping, t_1 exceeds $2t$, producing dispersionless and isolated flat edge bands, with its existence stemming from a zero Chern number, and a quantized fractional polarization term, i.e. $(P_x = 0, P_y = 1/2)$ due to the presence of in-plane mirror and chiral symmetries. While chiral symmetry-breaking parameters like spin-orbit coupling (SOC), onsite staggering, and the exchange proximity effect, threatens the FP-insulating phase, these terms can be utilized perturbatively to realize different configurations of topological-protected edge states (TESs), namely the vanishing helical, spin-polarized, and chiral TESs. In particular, this is shown by systematically adding these aforementioned terms while tracking its underlying symmetries and its zero-energy modes. Due to the existence of delocalized states around the $k_x = 0$ momenta, the finite size effect, which can destroy the quantum spin and

anomalous hall effect [38, 39], can be exploited to produce a helical and chiral TES spectrum, not possible through the chiral symmetry-breaking terms. Finally, the tunability of TESs can provide new avenues in designing electronic devices [25] and heterojunctions[43, 44], and also yield unusual behaviors in physical mechanisms such as in electron emission [45–48] and transport [23, 25].

Tier 2 Award (MOE-T2EP50221-0019). L.K.A. is supported by the ASTAR AME IRG (A2083c0057). W.J.C acknowledge the support of MOE PhD RSS.

ACKNOWLEDGMENT

Y.S.A. and P.F. are supported by the Ministry of Education, Singapore, under its Academic Research Fund

Appendix A: Full Hamiltonian

The bulk energy spectrum of this lattice model is obtained from the addition of Eqs. (1) to (4) s.t.

$$H_{\mathbf{k}} = \begin{bmatrix} f_{\text{SO}} + \lambda_{\text{AFM}} + \lambda_{\Delta} + \lambda_{\text{FM}} & f_1 - if_2 & 0 & g_1 - ig_2 \\ f_1 + if_2 & -f_{\text{SO}} - \lambda_{\text{AFM}} - \lambda_{\Delta} + \lambda_{\text{FM}} & (g_1 + ig_2)^{\dagger} & 0 \\ 0 & g_1 + ig_2 & -f_{\text{SO}} - \lambda_{\text{AFM}} + \lambda_{\Delta} - \lambda_{\text{FM}} & f_1 - if_2 \\ (g_1 - ig_2)^{\dagger} & 0 & f_1 + if_2 & f_{\text{SO}} + \lambda_{\text{AFM}} - \lambda_{\Delta} - \lambda_{\text{FM}} \end{bmatrix}, \quad (\text{A1})$$

with the following terms in Eqs. (6) to (8) and

$$g_1 = i\lambda_{\text{R}} \left(e^{ik_y a} - e^{-\frac{ik_y a}{2}} \cos\left(\frac{\sqrt{3}k_x a}{2}\right) \right); \quad g_2 = \sqrt{3}\lambda_{\text{R}} e^{-\frac{ik_y a}{2}} \sin\left(\frac{\sqrt{3}k_x a}{2}\right). \quad (\text{A2})$$

As discussed in Section III, the effect of RSOC is miniature and does not produces a new TESs configuration in agreement with [17] for the two helical TESs and hence, can be ignored.

Appendix B: Derivation of Edge States

The edge states are obtained by applying a semi-open boundary condition (sOBC) along k_y s.t. the system becomes a semi-infinite ZZ nanoribbon. Next, the NN hoppings from Eq. (A1) are decomposed into two hopping directions with respect to the ZZ edge - longitudinal and transverse. For l -th unit cell and width index m as defined in Fig. 1, Eq. (A1) can be decomposed into $H_{\text{L}} + H_{\text{T}} + H_{\text{SOC}}$ with

$$\begin{aligned} H_{\text{L}} &= t \sum_l \sum_{m=1}^N c_{l,A}^{\dagger}(m) c_{l-1,B}(m) + c_{l,B}^{\dagger}(m) c_{l,A}(m) + \text{h.c.}, \quad H_{\text{T}} = t_1 \sum_l \sum_{m=1}^{N-1} c_{l,A}^{\dagger}(m+1) c_{l,B}(m) + \text{h.c.}; \\ H_{\text{SO}} &= i\lambda_{\text{SO}} \sum_{l,s,s'} \nu \left(\sum_{m=1}^{N-1} \left[c_{l,A}^{\dagger}(m+1) \mathbf{s}_z^{s,s'} c_{l,A}(m) + c_{l+1,A}^{\dagger}(m+1) \mathbf{s}_z^{s,s'} c_{l,A}(m) \right] + \sum_{m=1}^N c_{l+1,A}^{\dagger}(m) \mathbf{s}_z^{s,s'} c_{l,A}(m) \right) \\ &\quad + (A \rightarrow B) + \text{h.c.} ((m+1 \rightarrow m-1) \ \& \ (l+1 \rightarrow l-1)), \end{aligned}$$

where H_{SO} is the intrinsic SOC NNN hopping terms with each line representing different NNN hoppings between sublattice A and B. This is repeated with its hermitian conjugate terms between width index $m-1$ and m , and unit cell $l-1$ and l , giving us a total of six NNN terms with its corresponding vector orientation defined as $\nu = \pm 1$. Additionally, the inclusion of staggering onsite potential, magnetic proximity effect and the RSOC is

$$H_{\text{stag}} = \sum_l \sum_{m=1}^N \lambda_{\Delta} c_{l,A}^{\dagger}(m) c_{l,A}(m) + (A \rightarrow B), \quad H_{\text{Ex}} = \sum_l \sum_{m=1}^N \lambda_{\text{Ex}} c_{l,A}^{\dagger}(m) \mathbf{s}_z^{s,s'} c_{l,A}(m) + (A \rightarrow B).$$

where the \mathbf{d} vector is similar to \mathbf{d}_{ij} in the bulk Hamiltonian. A block diagonal matrix of size $2N \in 4\mathbb{Z}$, i.e. $H_{2N}^{\text{edge}} = \text{diag}([H_{\uparrow}^{\text{edge}}]_N, [H_{\downarrow}^{\text{edge}}]_N)$ can be obtained by applying a Fourier transform along k_x with periodic boundary conditions (PBC) on the total Hamiltonian define in Section II with $c_i = \sum_k e^{ik_x \cdot x_{i,(A,B)}} c_{\mathbf{k}}(m) / \sqrt{L_x}$, $e^{ik_x L_x} = 1$ and $k_x = 2\pi m / L_x$ with $m \in \{0, 1, \dots, L_x\}$ and in the basis of $(c_{1,\uparrow}, c_{2,\uparrow} \dots c_{N,\uparrow}, c_{1,\downarrow} \dots c_{N,\downarrow})^T$. This allows us to get Eq. (13) in Section II.

The set of equations of motion (EOM) can be obtained by inserting a one-particle state [49],

$$|\Psi\rangle = \sum_m \left(\psi_{m,A} c_{A,k}^{\dagger}(m) + \psi_{m,B} c_{A,k}^{\dagger}(m) \right) |0\rangle, \quad (\text{B1})$$

where $c_{(A,B)}^{\dagger} |0\rangle = 0$, with $|0\rangle$ being the vacuum state, into $H |\Psi\rangle = \varepsilon_k |\psi\rangle$ s.t.

$$\varepsilon_k \psi_{m,A} = s_0 (f_{\text{NN}} \psi_{m,B} + t_1 \psi_{m-1,B} + \lambda_{\Delta} \psi_{m,A}) + s_z ((f_{\text{SO}} + \lambda_{\text{Ex}}) \psi_{m,A} + g_{\text{SO}} (\psi_{m+1,A} + \psi_{m-1,A})); \quad (\text{B2})$$

$$\varepsilon_k \psi_{m,B} = s_0 (f_{\text{NN}} \psi_{m,A} + t_1 \psi_{m+1,A} + \lambda_{\Delta} \psi_{m,B}) + s_z ((f_{\text{SO}} + \lambda_{\text{Ex}}) \psi_{m,B} + g_{\text{SO}} (\psi_{m+1,B} + \psi_{m-1,B})), \quad (\text{B3})$$

where λ_{Ex} can denote either the FM or AFM exchange.

Hence, the corresponding edge state Hamiltonian in the basis of $\{\psi_{1,A}, \psi_{1,B}, \dots, \psi_{N,A}, \psi_{N,B}\}$ is shown in Eq. (13). The finite termination at the zz edge at width index 0 and $N+1$ on sublattice B and A respectively impose the boundary condition of $\psi_{0,B} = \psi_{N+1,A} = \psi_{0,A} = \psi_{N+1,B} = 0$ and modifies the EOM s.t.

$$\varepsilon_k \psi_{1,A} = s_0 (f_{\text{NN}} \psi_{1,B} + \lambda_{\Delta} \psi_{1,A}) + s_z ((f_{\text{SO}} + \lambda_{\text{Ex}}) \psi_{1,A} + g_{\text{SO}} \psi_{2,A}); \quad (\text{B4})$$

$$\varepsilon_k \psi_{N,A} = s_0 (f_{\text{NN}} \psi_{N,B} + t_1 \psi_{N-1,B} + \lambda_{\Delta} \psi_{N,A}) + s_z ((f_{\text{SO}} + \lambda_{\text{Ex}}) \psi_{N,A} + g_{\text{SO}} \psi_{N-1,A}); \quad (\text{B5})$$

$$\varepsilon_k \psi_{1,B} = s_0 (f_{\text{NN}} \psi_{1,A} + t_1 \psi_{2,A} + \lambda_{\Delta} \psi_{1,B}) + s_z ((f_{\text{SO}} + \lambda_{\text{Ex}}) \psi_{1,B} + g_{\text{SO}} \psi_{2,B}); \quad (\text{B6})$$

$$\varepsilon_k \psi_{N,B} = s_0 (f_{\text{NN}} \psi_{N,A} + \lambda_{\Delta} \psi_{N,A}) + s_z ((f_{\text{SO}} + \lambda_{\text{Ex}}) \psi_{N,B} + g_{\text{SO}} \psi_{N-1,B}). \quad (\text{B7})$$

- [1] D. J. Thouless, M. Kohmoto, M. P. Nightingale, and M. den Nijs, Quantized Hall Conductance in a Two-Dimensional Periodic Potential, *Phys. Rev. Lett.* **49**, 405 (1982).
- [2] C. L. Kane and E. J. Mele, Z₂ Topological Order and the Quantum Spin Hall Effect, *Phys. Rev. Lett.* **95**, 146802 (2005).
- [3] X.-L. Qi, Y.-S. Wu, and S.-C. Zhang, General theorem relating the bulk topological number to edge states in two-dimensional insulators, *Phys. Rev. B* **74**, 045125 (2006).
- [4] F. Liu and K. Wakabayashi, Novel Topological Phase with a Zero Berry Curvature, *Phys. Rev. Lett.* **118**, 076803 (2017).
- [5] H. C. Wu, L. Jin, and Z. Song, Nontrivial topological phase with a zero Chern number, *Phys. Rev. B* **102**, 035145 (2020).
- [6] W. A. Benalcazar, B. A. Bernevig, and T. L. Hughes, Quantized electric multipole insulators, *Science*. **357**, 61 (2017).
- [7] M. Ezawa, Minimal models for Wannier-type higher-order topological insulators and phosphorene, *Phys. Rev. B* **98**, 045125 (2018).
- [8] J. Zak, Berry's phase for energy bands in solids, *Phys. Rev. Lett.* **62**, 2747 (1989).
- [9] W. A. Benalcazar, B. A. Bernevig, and T. L. Hughes, Electric multipole moments, topological multipole moment pumping, and chiral hinge states in crystalline insulators, *Phys. Rev. B* **96**, 245115 (2017).
- [10] L. Yang, A. Principi, and N. R. Walet, Wannier topology and quadrupole moments for a generalized Benalcazar-Bernevig-Hughes model, *Phys. Rev. B* **107**, 75413 (2023).
- [11] T. Fukui and Y. Hatsugai, Entanglement polarization for the topological quadrupole phase, *Phys. Rev. B* **98**, 035147 (2018).
- [12] J. F. Wienand, F. Horn, M. Aidelsburger, J. Bibo, and F. Grusdt, Thouless Pumps and Bulk-Boundary Correspondence in Higher-Order Symmetry-Protected Topological Phases, *Phys. Rev. Lett.* **128**, 246602 (2022).
- [13] H. Ma, Z. Zhang, P.-H. Fu, J. Wu, and X.-L. Yu, Electronic and topological properties of extended two-dimensional Su-Schrieffer-Heeger models and realization of flat edge bands, *Phys. Rev. B* **106**, 245109 (2022).
- [14] C.-A. Li, S.-J. Choi, S.-B. Zhang, and B. Trauzettel, Dirac states in an inclined two-dimensional Su-Schrieffer-Heeger model, *Phys. Rev. Res.* **4**, 023193 (2022).
- [15] C.-A. Li, S.-B. Zhang, J. C. Budich, and B. Trauzettel, Transition from metal to higher-order topological insulator driven by random flux, *Phys. Rev. B* **106**, L081410 (2022).
- [16] T. Kameda, F. Liu, S. Dutta, and K. Wakabayashi, Topological edge states induced by the Zak phase in A₂B₃ monolayers, *Phys. Rev. B* **99**, 075426 (2019).
- [17] S. Mondal and S. Basu, Vanishing of the quantum spin Hall phase in a semi-Dirac Kane-Mele model, *Phys. Rev. B* **105**, 235409 (2022).
- [18] S. Mondal and S. Basu, Topological phases of a semi-Dirac Chern insulator in the presence of extended range hopping, *Phys. Rev. B* **105**, 9 (2022).
- [19] M. Mecklenburg and B. C. Regan, Spin and the Honeycomb Lattice: Lessons from Graphene, *Phys. Rev. Lett.* **106**, 116803 (2011).
- [20] C. Qi, F. Jiang, and S. Yang, Advanced honeycomb de-

- signs for improving mechanical properties: A review, *Compos. Part B Eng.* **227**, 109393 (2021).
- [21] G. Montambaux, F. Piéchon, J.-N. Fuchs, and M. O. Goerbig, A universal Hamiltonian for motion and merging of Dirac points in a two-dimensional crystal, *Eur. Phys. J. B* **72**, 509 (2009).
- [22] G. Montambaux, F. Piéchon, J.-N. Fuchs, and M. O. Goerbig, Merging of Dirac points in a two-dimensional crystal, *Phys. Rev. B* **80**, 153412 (2009).
- [23] W. J. Chan, L. K. Ang, and Y. S. Ang, Quantum transport and shot noise in two-dimensional semi-Dirac system, *Appl. Phys. Lett.* **122**, 163102 (2023).
- [24] F. Zhai and J. Wang, Shot noise in systems with semi-Dirac points, *J. Appl. Phys.* **116**, 063704 (2014).
- [25] Y. S. Ang, S. A. Yang, C. Zhang, Z. Ma, and L. K. Ang, Valleytronics in merging Dirac cones: All-electric-controlled valley filter, valve, and universal reversible logic gate, *Phys. Rev. B* **96**, 245410 (2017).
- [26] S. Rostamzadeh and M. Sarisaman, Charge–pseudospin coupled diffusion in semi-Dirac graphene: pseudospin assisted valley transport, *New J. Phys.* **24**, 083026 (2022).
- [27] Y. W. Choi and H. J. Choi, Anisotropic pseudospin tunneling in two-dimensional black phosphorus junctions, *2D Mater.* **8**, 035024 (2021).
- [28] Y. Wu, A semi-Dirac point and an electromagnetic topological transition in a dielectric photonic crystal, *Opt. Express* **22**, 1906 (2014).
- [29] B. Real, O. Jamadi, M. Milićević, N. Pernet, P. St-Jean, T. Ozawa, G. Montambaux, I. Sagnes, A. Lemaître, L. Le Gratiet, A. Harouri, S. Ravets, J. Bloch, and A. Amo, Semi-Dirac Transport and Anisotropic Localization in Polariton Honeycomb Lattices, *Phys. Rev. Lett.* **125**, 186601 (2020).
- [30] J. P. Carbotte, K. R. Bryenton, and E. J. Nicol, Optical properties of a semi-Dirac material, *Phys. Rev. B* **99**, 15 (2019).
- [31] L. Mandhour and F. Bouhadida, Klein tunneling in deformed $\alpha - T_3$ lattice, [2004.10144](https://arxiv.org/abs/2004.10144) (2020).
- [32] E. Illes and E. J. Nicol, Klein tunneling in the $\alpha - T_3$ model, *Phys. Rev. B* **95**, 8 (2017).
- [33] P. Delplace, D. Ullmo, and G. Montambaux, Zak phase and the existence of edge states in graphene, *Phys. Rev. B* **84**, 195452 (2011).
- [34] M. Ezawa, Topological origin of quasi-flat edge band in phosphorene, *New J. Phys.* **16**, 115004 (2014).
- [35] C. Wang, Q. Xia, Y. Nie, M. Rahman, and G. Guo, Strain engineering band gap, effective mass and anisotropic Dirac-like cone in monolayer arsenene, *AIP Adv.* **6**, 035204 (2016).
- [36] C. Zhong, Y. Chen, Y. Xie, Y.-Y. Sun, and S. Zhang, Semi-Dirac semimetal in silicene oxide, *Phys. Chem. Chem. Phys.* **19**, 3820 (2017).
- [37] M. Alidoust, K. Halterman, D. Pan, M. Willatzen, and J. Akola, Strain-engineered widely tunable perfect absorption angle in black phosphorus from first principles, *Phys. Rev. B* **102**, 115307 (2020).
- [38] B. Zhou, H.-Z. Lu, R.-L. Chu, S.-Q. Shen, and Q. Niu, Finite Size Effects on Helical Edge States in a Quantum Spin-Hall System, *Phys. Rev. Lett.* **101**, 246807 (2008).
- [39] H.-H. Fu, J.-T. Lü, and J.-H. Gao, Finite-size effects in the quantum anomalous Hall system, *Phys. Rev. B* **89**, 205431 (2014).
- [40] D.-P. Liu, Z.-M. Yu, and Y.-L. Liu, Pure spin current and perfect valley filter by designed separation of the chiral states in two-dimensional honeycomb lattices, *Phys. Rev. B* **94**, 155112 (2016).
- [41] H. Ozawa, A. Yamakage, M. Sato, and Y. Tanaka, Topological phase transition in a topological crystalline insulator induced by finite-size effects, *Phys. Rev. B* **90**, 045309 (2014).
- [42] Y. Xu, Y. R. Chen, J. Wang, J. F. Liu, and Z. Ma, Quantized Field-Effect Tunneling between Topological Edge or Interface States, *Phys. Rev. Lett.* **123**, 206801 (2019).
- [43] Y. Betancur-Ocampo, Controlling electron flow in anisotropic Dirac materials heterojunctions: a superdiverging lens, *J. Phys. Condens. Matter* **30**, 435302 (2018).
- [44] G. Wang, J. Chang, W. Tang, W. Xie, and Y. S. Ang, 2D materials and heterostructures for photocatalytic water-splitting: a theoretical perspective, *J. Phys. D: Appl. Phys.* **55**, 293002 (2022).
- [45] Y. S. Ang, H. Y. Yang, and L. K. Ang, Universal Scaling Laws in Schottky Heterostructures Based on Two-Dimensional Materials, *Phys. Rev. Lett.* **121**, 056802 (2018).
- [46] Y. S. Ang, L. Cao, and L. K. Ang, Physics of electron emission and injection in two-dimensional materials: Theory and simulation, *InfoMat* **3**, 502 (2021).
- [47] W. J. Chan, C. Chua, Y. S. Ang, and L. K. Ang, Field Emission in Emerging Two-Dimensional and Topological Materials: A Perspective, *IEEE Trans. Plasma Sci.* , 1 (2022).
- [48] Y. Luo, Y. S. Ang, and L. K. Ang, Universal Model of Optical-Field Electron Tunneling from Two-Dimensional Materials, [2303.10879](https://arxiv.org/abs/2303.10879) (2023).
- [49] K. Wakabayashi, K.-i. Sasaki, T. Nakanishi, and T. Enoki, Electronic states of graphene nanoribbons and analytical solutions, *Sci. Technol. Adv. Mater.* **11**, 054504 (2010).